Mapping of sea ice concentration using the NASA NIMBUS 5 ESMR microwave radiometer data 1972-1977

Wiebke Margitta Kolbe[1,2], Rasmus T. Tonboe[1], and Julienne Stroeve[3,4,5]

[1]National Space Institute, Technical University of Denmark (DTU Space), DK-2800 Lyngby, Denmark
[2]Danish Meteorological Institute (DMI), Copenhagen, Denmark
[3]University of Manitoba, Winnipeg, Canada
[4]University College London (UCL), London, UK
[5]University Colorado, National Snow and Ice Data Center (NSIDC), Boulder, Colorado, USA

Correspondence: W. M. Kolbe (wmako@space.dtu.dk)

Abstract. The Electrically Scanning Microwave Radiometer (ESMR) instrument on board the NIMBUS 5 satellite was a one channel microwave radiometer measuring the 19.35 GHz horizontally polarised brightness temperature (T_B) from Dec. 11, 1972 to May. 16. 1977. The original tape archive data in swath projection have recently been made available online by NASA Goddard Earth Sciences Data and Information Services Center (GES DISC). Even though ESMR was a predecessor of modern

5   multi frequency radiometers, there are still parts of modern processing methodology which can be applied to the data to derive the sea ice extent globally.

Here we have reprocessed the entire data set using a modern processing methodology, that includes implementation of pre-processing filtering, dynamical tie-points, and a radiative transfer model (RTM) together with numerical weather prediction (NWP) for atmospheric correction. We present the one channel sea ice concentration (SIC) algorithm and the model for com-

10   puting temporally and spatially varying SIC uncertainty estimates. Post-processing steps include re-sampling to daily grids, land-spill-over correction, application of climatological masks, setting of processing flags and estimation of sea ice extent, monthly means and estimation of trends. This sea ice dataset derived from NIMBUS 5 ESMR extends the sea ice record with an important reference from the mid 1970s. To make a consistent analysis of the sea ice development through time easier, the same grid and landmask as for EUMETSAT's OSI-SAF SMMR based sea ice CDR have been used for our ESMR dataset. SIC

15   uncertainties have been included for further ease of comparison to other datasets and time periods.

We find that our sea ice extent in the Arctic and Antarctic in the 1970s is generally higher than those available from the National Snow and Ice Data Center (NSIDC) Distributed Active Archive Center (DAAC) derived from the same ESMR dataset, with mean differences of 240.000 and 590.000 km^2, respectively. The largest differences reach up to 2 million km^2, when comparing monthly sea ice extents. Such large differences cannot be explained by the different grids and landmasks of the

20   datasets alone, and must therefore also result from the difference in data filtering and algorithms, such as the dynamical tie-points and atmospheric correction.

The new ESMR SIC data set has been released as part of the ESA Climate Change Initiative Programme (ESA CCI) and is publicly available at: http://dx.doi.org/10.5285/34a15b96f1134d9e95b9e486d74e49cf (Tonboe et al., 2023).

1 Introduction

Several sea ice concentration (SIC) algorithms have been developed for passive microwave data (PMW), differing in the usage of e.g. frequencies and polarizations of the PMW data (Comiso et al., 1997), or the usage of static or dynamic tie-points (Parkinson et al., 2004; Tonboe et al., 2016; Lavergne et al., 2019). From the resulting data sets, it becomes apparent that the arctic sea ice extent (SIE) in September has been decreasing at a rate of about 12 percent per decade since the launch of modern satellite multi-frequency microwave radiometers in 1978 (Onarheim et al., 2018; Stroeve and Notz, 2018). This negative sea ice trend in the Northern Hemisphere already started in the 1970s (Rayner et al., 2003; Walsh et al., 2017), though regional trends can differ, as seen for example within the Barents Sea (Chapman and Walsh, 1991). In the Antarctic there are large regional differences in SIE trends but until recently, the overall trend was positive due to sea ice dynamics (Turner et al., 2009; Sun and Eisenman, 2021). This has changed however in the last decade as a result of several record lows, and as such overall trends have shifted to a more homogeneous pattern, (Schroeter et al., 2023), and in summer (NDJF) the overall trends are now slightly negative. Until recently, the slightly positive trend was believed to be part of long term natural variability that overshadowed the effects of global warming starting in the 1960s (Wang et al., 2019; Stammerjohn et al., 2008; Thompson and Solomon, 2002; Ferreira et al., 2015; Singh et al., 2019; Fogt et al., 2022). In order to fully understand the drivers of sea ice variability, extending the sea ice data record backwards in time is essential.

Globally, SIE information prior to the satellite data record was largely from ice charts and ship observations. While there have been efforts to include this data in long-term assessments of sea ice change, the data are typically provided in relatively coarse spatial and temporal resolution (1 deg grid) (Walsh et al., 2019) interpolating in both time and space (Titchner and Rayner, 2014). Only satellite based data-sets offer the ability to cover both hemispheres at improved spatial and temporal resolutions, and generally have consistency in processing methods (Lavergne et al., 2019). SIC derived from Nimbus 5 Electrically Scanning Microwave Radiometer (ESMR) data was previously processed by Parkinson et al., 2004. Here we apply a new processing method that is comparable to the EUMETSAT/ESA CCI SIC record from 1978 and on-wards (see Andersen et al., 2006; Tonboe et al., 2016). Compared to Parkinson et al., 2004, this method reduces atmospheric noise regionally over both ice and water surfaces and uses the pre-processed data to develop a SIC algorithm calibration that is effective in removing both instrument drift and offsets. Seasonal sea ice signature variations are removed by using dynamical tie-points. Lastly, the algorithm calculates time and spatially varying uncertainty estimates.The ESMR SIC data are presented on the same grid and with the same masking as the EUMETSAT/ ESA CCI record, which makes these two records directly comparable. This and the modern processing chain mentioned above warrant the reprocessing presented in this article.

In the following Section 2, the satellite and reanalysis data are described, including the formatting and initial filtering of the data. Section 3 introduces the radiative transfer model (RTM) used for the atmospheric correction, while Section 4 describes the dynamical tie-points, the SIC algorithm with uncertainty estimations, the land-spill-over method and data flags assigned during post-processing. In Section 5, the resulting SIC dataset is presented and compared to other datasets. Finally, Section 6 consists of a discussion and Section 7 provides the conclusions of this work.

2 The NIMBUS 5 ESMR instrument and data

The NIMBUS 5 ESMR instrument was a cross-track scanner measuring at 78 scan positions perpendicular to the flight track with a maximum incidence angle of about 64 degrees to both sides (NASA GSFC, 2016). No direct observations at nadir have been made, the closest positions being at +/- 0.7 degrees. The near circular orbit height was about 1112 km with an inclination of 81 degrees. The phased array antenna dimensions was 85.5 x 83.3 cm and the spatial resolution about 25 km near nadir increasing to about 160 x 45 km at the edges of the swath (NASA GSFC, 2016). The full swath was about 3100 km with varying incidence angle and spatial resolution giving a very good (unprecedented) daily coverage in polar regions with no gaps, i.e. no pole holes. The ESMR onboard the NIMBUS 5 satellite was a one channel 19.35 GHz horizontally polarised microwave radiometer operating from 11. December 1972 until 16. May 1977 (1617 days) with some interruptions (see list of days with missing files in Appendix A2). Due to a hot-load anomaly, there are major data gaps between March to May and again in August 1973. Another major data gap occurred from 3 June 1975 until 14 September 1975 because the ground segment was used for receiving Nimbus 6 data instead (Parkinson et al., 1999). When resuming operation in September 1975 the instrument was only operated approximately every other day. From late 1976 to the end of the mission, operation was highly irregular. The last file in the data-set is from 16 May 1977. The data have recently been made available online by NASA in the original tape archive format (TAP-files).

2.1 Formatting and co-location of brightness temperatures and ECMWF ERA5 data

The ESMR data were retrieved from the NASA Goddard Earth Sciences Data and information services center (GES DISC) on-line data archive (NASA GSFC, 2016).This data set contains, along with a number of instrument and geographical parameters, 19.35 GHz calibrated brightness temperatures expressed in units of Kelvin. The raw data was recovered by NASA from the magnetic tapes, called Calibrated Brightness Temperature Tapes (CBTT), where they were stored in the original binary TAP file format, each file corresponding to a particular orbit (NASA GSFC, 2016).

All variables in the TAP files were read using online NASA software and converted to NetCDF format without changing the original data structure, creating raw ESMR NetCDF files. Each data point in the TAP file was matched with European Centre for Medium Range Weather Forecast (ECMWF) ERA5 re-analysis data (Bell et al., 2020; Hersbach et al., 2020) in time and space (nearest) and appended to the raw ESMR NetCDF file, serving as input to the processing chain. The resulting data are structured in arrays line by line (across-track). Appendix A1 summarizes the variables included in the NetCDF files.

2.2 Initial filtering and correction of brightness temperatures

NASA provides a correction on the brightness temperature data to account for lobe structure, antenna loss and angular T_B variation (NASA CR, 1974). According to NASA the correction was needed because: "The cause of the gross variations in antenna properties which were observed soon after launch has been determined to be a cross-polarized grating lobe [. . .] The problem does not exist for the near-nadir beam positions so these positions are unaffected. [. . .] An empirical calibration has

been developed which removes the effect of the lobe structure and antenna loss, which vary with position, and roughly corrects for angular variations in viewing geometry." (NASA CR, 1974, p.400).

90 Originally, it was planned to use only lobe corrected T_Bs with their natural angular dependency, but we did not find a way to extract this in the NASA provided data-set. Essentially, only the combined lobe and angular correction, which is a function of brightness temperature, can be removed altogether from the data NASA provides. Thus, the T_Bs do not vary as a function of incidence angle, as would be expected for T_Bs from the sea surface and sea ice.

Despite the corrections done by NASA, the ESMR data still contain erroneous T_Bs, scan-lines, sudden jumps in the calibra-
95 tion and other obvious artifacts.

Since the ESMR data contains corrupted data and erroneous scan-lines, filtering is needed before the data can be used for sea ice mapping. The filters that we apply are described in Eqns 1-4. They are applied in the same order as described here and if only a single data point or a couple of scan lines are affected only these data points and scan lines are removed from the file. If the whole file is corrupted then it is deleted.

100 An initial analog filter is used for filtering erroneous T_Bs and scanlines. The filter is based on the 16 analog voltage entries in the data. The NIMBUS 5 ESMR user's guide (Sabatini, 1972) does not explain very well what the 16 entries really are, or what unit the voltages are stored in, but jumps in these analog signals correspond to anomalous T_Bs. Our analog filter computes the absolute gradient in the analog signals and anything over a value of 10 is removed. This threshold was estimated experimentally.

105 Next, several other filters are employed using the processed T_B (in Kelvin) from the previous step. The filters are applied in the following order:

Data that are non-physical and outside the expected range for sea and ice surfaces are removed. Only data points that lie inside the range specified in Eq. 1 are kept:

$$90K < T_B \leq 273.15K \tag{1}$$

110 The next filter removes erroneous scan-lines (across track rows). Consecutive scan-lines should not differ by more than 50K as shown in Eq. 2. The threshold of 50K was estimated experimentally.

$$\frac{\sum_j^n |T_{B_{j,i+1}} - T_{B_{j,i}}|}{n} \leq 50K \tag{2}$$

where T_{B_i} in Eq. 2 is an across track row of T_B and i is an index along track, while j is an index across track. n is the maximum across track index of a row, i.e. for a complete row with valid data points for all 78 incidence angles $n = 78$.

115 Afterwards, single T_B outliers are removed, if they cannot satisfy Eq. 3:

$$|p_i - p_{i-1}| + |p_{i+1} - p_i| \leq 150K \tag{3}$$

where p is a single pixel T_B and i is an along track index. The threshold of 150K was selected manually after identifying erroneous single pixel outliers in the data. The last filter in Eq. 4 removes neighbouring T_Bs which are locked on the same value, i.e. T_Bs for which the following equation equals zero:

120 $$|p_{i+6} - p_{i+5}| + |p_{i+5} - p_{i+4}| + |p_{i+4} - p_{i+3}| + |p_{i+3} - p_{i+2}| + |p_{i+2} - p_{i+1}| + |p_{i+1} - p_i| \neq 0 \tag{4}$$

where p is again a single pixel T_B with an along track index i. The choice of comparing 7 consecutive T_Bs is based on qualitative experiments. Since the filter is used universally for all incidence angles, the search window varies but covers a minimum distance of 175 km.

The outer data points of the swath edges showed significant higher noise levels and coarser resolution than the near nadir data points (Veng, 2021). Therefore, after the filtering we additionally remove the 4 outermost data points of the swath, corresponding to incidence angles between 57 and 64 degrees on both sides. The new outer edges of the swath data is then at ∼56 degrees, similar to modern microwave radiometers for sea ice retrieval of 50-55 degrees (AMSR (Meisner and Wentz, 2000), SMMR (Wentz, 1983), SSM/I (Wentz, 1997)).

Before the filtering, the dataset contained 13496 orbital data files; after filtering there are 10649 (∼79%) good files left. A complete list of days where data are missing after filtering and no SIC could be retrieved is given in appendix A3.

3   The radiative transfer model

The Radiative Transfer Model (RTM) has been developed specifically for atmospheric noise reduction and it is comparable to the RTM's used in Andersen et al., 2006 and Tonboe et al., 2016 but with the addition that this ESMR RTM (Eq. 5) can be applied for different incidence angles over both ocean and ice. The RTM takes as input: atmospheric columnar water vapor V [mm or kgm^{-2}], 10 m wind speed W [ms^{-1}], atmospheric columnar cloud liquid water L [mm or kgm^{-2}], sea surface temperature Ts [K], ice emitting layer temperature Ti [K], sea ice concentration c_{ice} [0-1], and incidence angle [deg]. In return, it simulates the top-of-the-atmosphere 19.35 GHz T_B at horizontal polarisation.

$$T_B = RTM(V, W, L, T_s, T_i, c_{ice}, \theta) \tag{5}$$

The RTM uses the atmospheric part of the model described in (Wentz, 1997) to compute atmospheric emission, transmissivity and reflectivity at the sea surface (open water) together with added modules for simulating the sea ice emissivity (Fig. 1) and open water reflectivity as a function of incidence angle.

For the sea ice emissivity, a look-up-table is produced from a simulation using a combined sea ice thermodynamic and emission model during Arctic winter on first-year ice. The thermodynamical and emission model set-up and the simulations are described in Tonboe, 2010. The emissivities as a function of incidence angle are shown in Figure 1 and the look-up-table is given in Table 1.

Incidence angle, θ , and first-year ice emissivity, E_{ice}													
θ	0	5	10	15	20	25	30	35	40	45	50	55	60	65
E_{ice}	0.91	0.91	0.91	0.91	0.90	0.90	0.89	0.89	0.88	0.86	0.85	0.83	0.80	0.77

Table 1. Sea ice emissivity look-up-table.

Sea water permittivity, which is used to estimate the calm sea reflectivity (Eq. 6) as a function of temperature, is computed using equation E64 (p. 2046) in Ulaby et al., 1986. The permittivity is almost invariant of the water salinity at 19 GHz and a constant value of 34 ppt is used here.
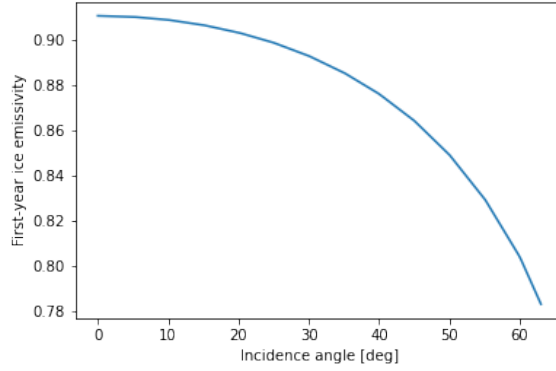
Figure 1. The first year-ice emissivity used in the RTM

The calm sea (Fresnel) power reflection coefficient, r_h, as a function of the relative permittivity, ϵ, and the incidence angle, θ, for a lossy medium, is computed using Eq. 1.52 in Schanda, 1986, i.e.

$$r_h(\theta) = \frac{(p - cos(\theta))^2 + q^2}{(p + cos(\theta))^2 + q^2}, \tag{6}$$

where p and q are abbreviations for:

$$p = \frac{1}{\sqrt{(2)}}((\epsilon'_r - sin^2\theta)^2 + \epsilon''^2_r)^{\frac{1}{2}} + (\epsilon'_r - sin^2\theta))^{\frac{1}{2}} \tag{7}$$

and

$$q = \frac{1}{\sqrt{(2)}}((\epsilon'_r - sin^2\theta)^2 + \epsilon''^2_r)^{\frac{1}{2}} - (\epsilon'_r - sin^2\theta))^{\frac{1}{2}} \tag{8}$$

where the relative permittivity $\epsilon_r = \epsilon'_r + \epsilon''_r j$ of the water surface is a complex number. The calm sea emissivity, E_0, is then

$$E_0 = 1 - r_h. \tag{9}$$

The rough water surface emissivity component, E_W, is added to the calm sea emissivity, E_0, to produce the total sea water emissivity, E_{water}. Between ESMR incidence angles of 0 and 63 degrees the 19.35 GHz horizontal polarization E_W sensitivity to wind speed is an almost a linear function ($\frac{\Delta(E_W T_s)}{\Delta W} = 0.0094\theta + 0.3$) of incidence angle, θ, (Meisner and Wentz, 2012), i.e.

$$E_W = \frac{W(0.0094\theta + 0.3)}{T_s}, \tag{10}$$

and

$$E_{water} = E_0 + E_W \tag{11}$$

where θ is the incidence angle in degrees, W is the wind speed, and T_s is the sea surface temperature [K].

This combination of E_0 and E_W follows the procedure described in (Wentz, 1997).

The resulting brightness temperature is a linear combination of the sea water and sea ice emission weighted by the SIC following Andersen et al., 2006.

170 $$T_B = T_{BU} + \tau((1-c_{ice})E_{water}*T_s + (1-c_{ice})(1-E_{water})(\Omega T_{BD} + \tau T_{BC}) + c_{ice}E_{ice}T_i + c_{ice}(1-E_{ice})(T_{BD} + \tau T_{BC})) \quad (12)$$

where T_{BU} is the up-welling brightness temperature from the atmosphere, τ the atmospheric transmissivity, E_{water} the water surface emissivity, E_{ice} the sea ice emissivity, Ω the reflection reduction factor due to water surface roughness, T_{BD} the down-welling brightness temperature, and T_{BC} the cosmic background brightness temperature (2.7 K).

EMSR-simulated $T_B s$ and emissivities have been compared with other simulated $T_B s$ using other RTMs for AMSR (Meisner
175 and Wentz, 2000), SMMR (Wentz, 1983), SSM/I (Wentz, 1997) for a constant incidence angle of 55 degrees, which is close to the incidence angle of the other instruments and RTMs (53-55 degrees). The comparison showed that the $T_B s$ of the ESMR RTM are within the same range (approx. 2K) of values of the other models and therefore it seems to be reasonable given the differences in instruments centre frequency and measurement geometry. It is noted that in the correction procedure, differences between two simulated $T_B s$ are used to minimize model biases. Even if the absolute values of the RTM simulated $T_B s$ are
180 biased, this bias would be removed by taking the difference between two simulated $T_B s$, which is the only part used in the correction.

4 Derivation of sea ice concentration

The RTM is an essential part of the SIC derivation for applying an atmospheric noise reduction. The following section presents the calculations of dynamical tie-points and the SIC algorithm, along with uncertainty estimations. Lastly, the post-processing,
185 including land-spill-over method and data flags assignments, is described. A flow-chart illustrating this processing chain can be found in the ESA CCI ESMR product user guide (PUG) (ESA CCI, 2022).

4.1 Tie-points and geophysical noise reduction

Tie-points are typical signatures of 100 % ice and open water (0 % ice) and are used in SIC algorithms as a reference for estimating the total ice fraction per satellite pixel c_{ice}. Using dynamical tie-points aims to reduce SIC biases that may result
190 from seasonal and inter annual variations of $T_B s$ (Kongoli et al., 2011), instrument drift and RTM and ERA5 biases. For example, (Comiso and Zwally, 1980) argue that the variations in average open water $T_B s$ near the ice edge are affected primarily by variations in instrument calibration, and they describe the drop followed by a sharp increase seen in Figure 2 in 1975 as an instrument drift issue.

Our ESMR tie-points are derived on a daily basis from the swath files. Regions of open water and high SICs are selected for
195 each hemisphere, resulting in two regions of sea ice and two of open water for both hemispheres. The ERA5 SIC prior to 1979 is based on the HadISST2.0.0.0 data set (Bell et al., 2021), which mainly utilizes digitized sea ice charts for this period (Rayner

et al., 2003). The two main data sources are the Walsh data set (Walsh, 1978; Walsh and Johnson, 1979; Walsh and Chapman, 2001) and National Ice Center (NIC) charts (Knight, 1984). The data sets also consist of several data types besides ice charts, e.g. ship observations and satellite data, both infrared and microwave observations, including data from ESMR. The selection of the four tie-points is based on a criteria set for SIC from ERA5, distance from ice edge, observed brightness temperature, latitude and sea surface temperature, shown in table 2.The distance from ice edge criterium is imposed by putting a threshold on the mean SIC of a 5 x 5 grid point box, which for ice tie points should be larger than 80% or less than 1% for open water points. While computed daily, these are subsequently combined into 15-day running mean tie-points, 7 days ahead and 7 days behind the processed date shown in Figure 2. The 15-day averaging period has been maintained even at the beginning and end of the data-set and when there are data gaps, i.e. if there are gaps, the averaging is done over the days available in the 15-day period, also in the beginning, where the first 7 days are missing. Figure 2 depicts the 15-day averaged tie-points through time. It shows that the ice tie-points follow a seasonal pattern, while the water tie-points are relatively constant. The tie-point criteria from table 2 ensure that each daily tie-point is based on many observations, which result in stable tie-points. The 15-day interval has been chosen experimentally, so the TB variations seem reasonable and one is still able to identify calibration issues as jumps as e.g. in 1976.

	Ice	Ocean

Arctic	90 >latitude >32
	sea ice concentration (ERA5) >0.8
	mean sea ice concentration (ERA5) of
	    a 5 x 5 grid point box >0.8
	100 K <brightness temperature <274 K
		90 >latitude >32
		sea ice concentration (ERA5) = 0
		mean sea ice concentration (ERA5) of
		    a 5 x 5 grid point box <0.01
		sea surface temperature (ERA5) >278 K
		90 K <brightness temperature <180 K

Antarctic	-90 <latitude <-48
	sea ice concentration (ERA5) >0.8
	mean sea ice concentration (ERA5) of
	    a 5 x 5 grid point box >0.8
	100 K <brightness temperature <274 K
		-90 <latitude <-48
		sea ice concentration (ERA5) = 0
		mean sea ice concentration (ERA5) of
		    a 5 x 5 grid point box <0.01
		sea surface temperature (ERA5) >278 K
		90 K <brightness temperature <180 K

Table 2. Criteria for the four different tie-points.

The per grid-point T_B correction term $\Delta T_{B,simulated}$, is the difference between a simulated reference T_B using mean values of total column water vapor [kg/m^2] in the atmosphere ($\overline{V}$), 10 m wind speed [m/s] ($\overline{W}$), total column cloud liquid water
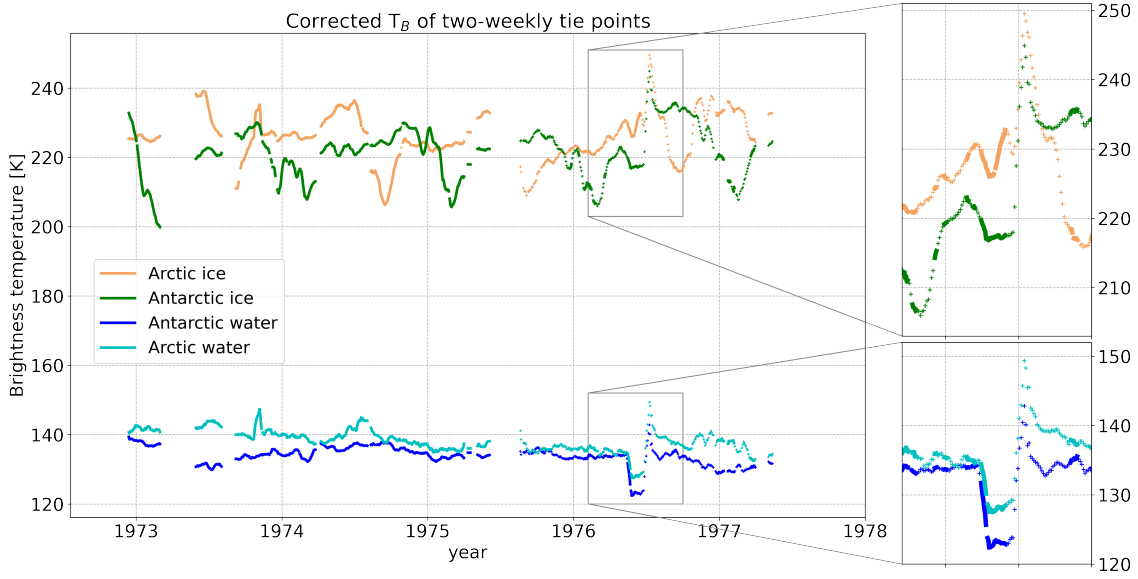
Figure 2. The two-weekly tie-points for Arctic and Antarctic ice and water after T_B correction. The boxes are showing the period during May-July 1976 with obvious instrument calibration issues.

$[kg/m^2]$ in the atmosphere ($\overline{L}$), the sea surface temperature ($\overline{T_s}$), the ice emitting layer temperature ($\overline{T_i}$) as input to the RTM and a simulated T_B using the actual ERA5 values $(V, W, \overline{L}, T_s, T_i)$ for the grid-point. The T_B is not corrected for cloud liquid water, L, so the mean L is input to both the reference and the actual simulation. $\Delta T_{B,simulated}$ can both be negative and positive and after correction, the T_Bs have reduced sensitivity to the geophysical noise sources: V, W, T_s, T_i. The fact that the correction term is the difference between two RTM simulations minimizes the impact of biases in the model and the ERA5 data.

The correction term is added to the measured T_B, i.e.

$$T_{B,corrected} = T_{B,measured} + \Delta T_{B,simulated}, \tag{13}$$

where

$$\Delta T_{B,simulated} = RTM(\overline{V}, \overline{W}, \overline{L}, \overline{T_s}, \overline{T_i}, c_{ice}, \theta) - RTM(V, W, \overline{L}, T_s, T_i, c_{ice}, \theta) \tag{14}$$

where $c_{ice} = 0$ is the open water tie-point and $c_{ice} = 1$ the ice tie-point. Following (Svendsen et al., 1983), T_i is computed as:

$$T_i = 0.4 \cdot T_{2m} + 0.6 \cdot 272, \tag{15}$$

where T_{2m} is the 2 m air temperature, which is taken from the ERA5 data. The horizontal bars above the variable indicate that they are daily mean values for cluster of points selected for the tie-point. The mean water vapor, $\overline{V}$ in the tie-point is shown in Figure 3.
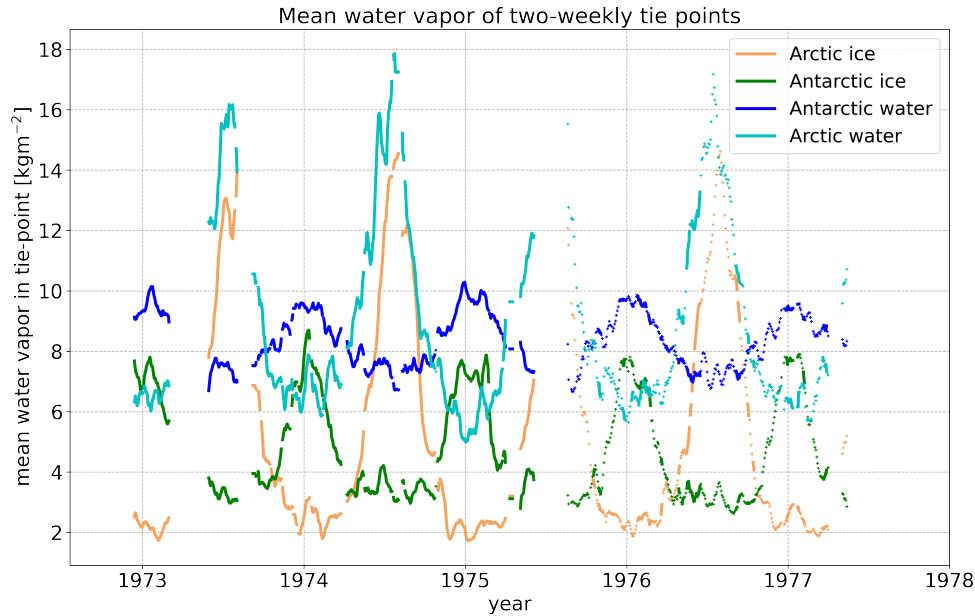
Figure 3. Mean Atmospheric water vapor for all grid points included in the four tie-points. Water vapor data from ERA5 (Hersbach et al., 2020).

Figure 4 shows the correction term, $\Delta T_{B,simulated}$, Jan. 1., 1974 over open water in the Northern and Southern Hemisphere respectively. The path-length through the atmosphere is longest at high incidence angles and shortest near nadir, and thus, the absolute value of the correction is largest at high incidence angles. For example, when the atmosphere is driest in the reference compared to the actual simulation, the ends of the corrected T_B turn negative, while they turn strongly positive when the reverse is true.

The correction works best over open water areas, where it acts as only an atmospheric correction. The RTM appears to better simulate the relevant emission processes in the atmosphere, and the ERA5 data more accurately quantifies the atmospheric noise sources. Over sea ice, geophysical noise sources are related to processes in the snow and ice profile (Tonboe et al., 2021) which are not characterised by the RTM except for the emitting layer temperature T_i. The T_i, which is used as input to the RTM, is estimated from the 2 meter air temperature in the ERA5 data using Eq. 15. This is important because ESMR is a single channel instrument and thus the T_B and also the derived c_{ice} are sensitive to emitting layer temperature.

The standard deviation of the brightness temperatures for water points in both hemispheres, before and after the correction, is shown in figure 5.

a)

b)
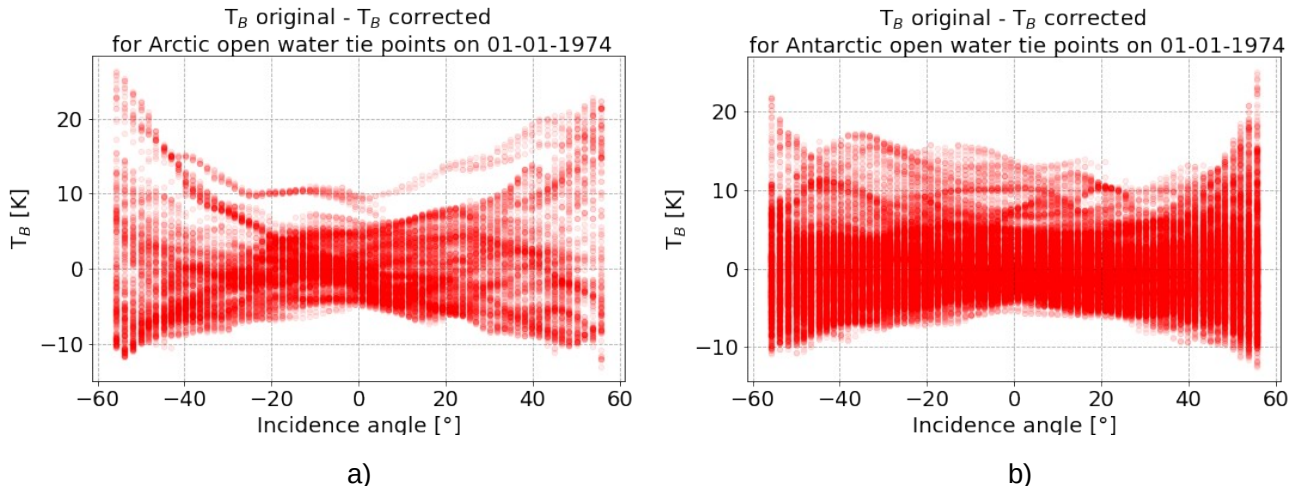
Figure 4. Difference of T_Bs before and after correction with a mean reference for open water tiepoints in the a) Northern Hemisphere and b) Southern Hemisphere.

a)

b)
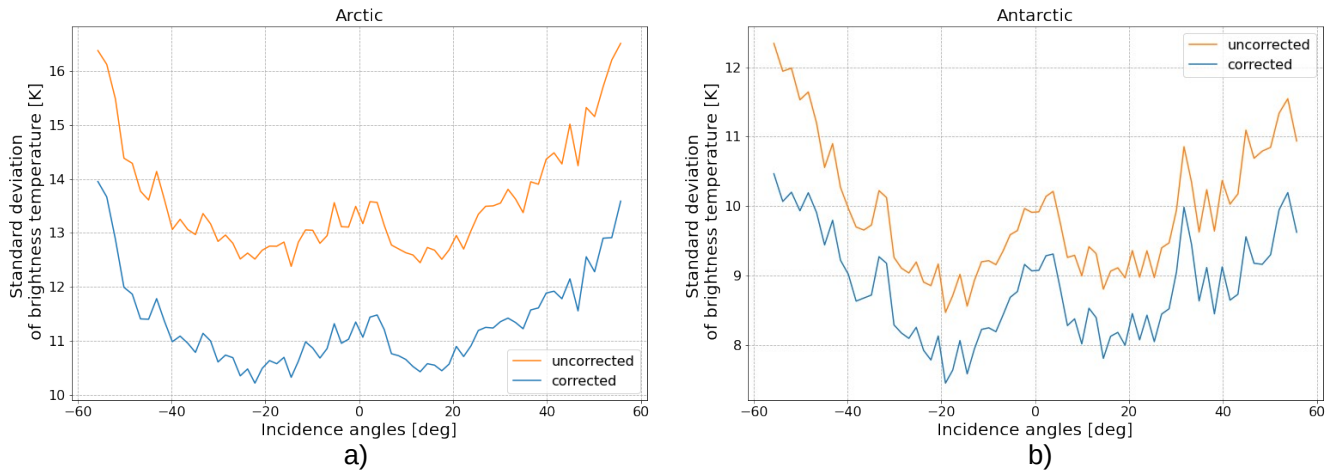
Figure 5. Standard deviations of T_Bs, before and after correction in January 1974 for the a) Northern Hemisphere and b) Southern Hemisphere. Only filtered for ocean points with ERA5 SIC and SST.

4.2 The sea ice concentration (SIC) and its uncertainty

SIC (c_{ice}) is estimated using the measured brightness temperature ($T_{B,measured}$) and the open water ($T_{p,water}$) and ice ($T_{p,ice}$) tie points, i.e.

$$c_{ice} = \frac{T_{B,measured} - T_{p,water}}{T_{p,ice} - T_{p,water}} \qquad (16)$$

245   Because the RTM requires c_{ice} as input, c_{ice} is processed iteratively in two steps:

    1) The c_{ice} is first estimated using uncorrected $T_B s$ and tie-points derived from uncorrected data. The c_{ice} estimate is truncated to the interval between 0 and 1 and an open water filter is applied, forcing all c_{ice} values less than 0.15 to 0.

    2) The c_{ice} estimate from step (1) is used in the RTM calculation (Eq. 5) together with ERA5 data for the geophysical noise reduction of the $T_B s$ and c_{ice} is then estimated again in a second iteration, this time using corrected $T_B s$ and corrected tie-

250   points. The mean values of $\overline{V}, \overline{W}, \overline{L}...$ used in the reference simulation is a weighted average with c_{ice} of the mean water and ice tie-point values respectively, i.e. c_{ice} is used as a ratio to mix the two tie-point values to create mean values of the NWP data for any sea ice concentration.

    Iterations to update c_{ice} could in principle continue. However, tests show that updates are small after one iteration and we only iterate once (e.g. Lavergne et al., 2019).

255   The total SIC uncertainty is the combination of two components: 1) algorithm uncertainty, which includes instrument noise and tie-point variability (geophysical noise) and 2) re-sampling uncertainty, which is uncertainty due to data re-sampling.

    The algorithm uncertainty is the squared sum of three independent components following Parkinson et al., 1987:

$$\delta c_{ice,algorithm} = ((\frac{\delta T_B}{T_{p,ice} - T_{p,water}})^2 + (\frac{-(1 - c_{ice})\delta T_{p,water}}{T_{p,ice} - T_{p,water}})^2 + (\frac{-c_{ice}\delta T_{p,ice}}{T_{p,ice} - T_{p,water}})^2)^{\frac{1}{2}} \tag{17}$$

    where the first term in eq. 17 represents variations due to instrument noise, estimated to a δT_B brightness temperature error

260   of 3 K (Parkinson et al., 1987).

    Without the instrument noise term, which is already included in the two tie-point uncertainties, the second and third term in eq. 17 are used to compute the algorithm uncertainty, $\delta c_{ice,algorithm}$:

$$\delta c_{ice,algorithm} = ((\frac{-(1 - c_{ice})\delta T_p, water}{T_{p,ice} - T_{p,water}})^2 + (\frac{-c_{ice}\delta T_{p,ice}}{T_{p,ice} - T_{p,water}})^2)^{\frac{1}{2}} \tag{18}$$

    where $\delta T_{p,water}$, is the water tie-point error, here the (one) standard deviation of the daily tie-point, $\delta T_{p,ice}$, is the ice tie-

265   point error (e.g. one standard deviation of the daily tie-point). The water and ice tie-point errors are weighted by the SIC, and all three errors are normalized with the ice - water brightness temperature contrast and the 2-weekly tie-points. The algorithm uncertainty is computed on swath data.

    The re-sampling uncertainty, $\delta c_{ice,re-sampling}$ is the maximum c_{ice}- minimum c_{ice} difference of a 3 x 3 pixel window. The re-sampling uncertainty is computed on re-sampled data (e.g. Lavergne et al., 2019).

270   The total uncertainty is the squared sum of the algorithm and the re-sampling uncertainty, i.e.

$$\delta c_{ice,total} = (\delta c_{ice,algorithm}^2 + \delta c_{ice,re-sampling}^2)^{\frac{1}{2}} \tag{19}$$

    The two uncertainty components and the total uncertainty are included in the data file.

4.3   Land-spill-over correction and post-processing

    Land-spill-over correction is following the procedure described in Markus and Cavalieri, 2009. A 5 by 5 pixel neighbourhood

275   of the land mask (EASE2 version 2, by OSI-SAF) is analysed to determine which coastal points should be corrected. The land

mask is divided into two classes: land points, which are given a value of 90% SIC and open ocean points. If the difference between the original land mask and the calculated mean mask by the 5 by 5 window is larger than the previously estimated SIC (the RTM corrected & re-sampled SIC), i.e. the SIC is smaller than the theoretical value of the land spill over only, the SIC value is set to 0% and the status flag variable of the data set is raised to 8.

Additionally, a monthly climatology (also by OSI-SAF, same version as land mask) is used to set SIC to 0% and mark open water points by a climatology boundary, which is indicated by a status flag value of 64. Afterwards the land mask is used to also mark lakes and coastal areas with status flags 2 and 32 respectively. An overview of all status flag values is shown in table 4:

Status flag values for SIC retrievals	
no flag/flag 0	Nominal retrieval by the SIC algorithm
flag 1	Land
flag 2	Lake
flag 4	SIC is set to zero by the open water filter
flag 8	SIC value is changed for correcting land spill-over effects
flag 16	Handle with caution, the 2m air temperature is high at this position, and this might be false ice
flag 32	Coast
flag 64	SIC is set to zero since position is outside maximum sea ice climatology
flag 128	Point not accepted but no other flags raised

Table 4. Description of the $status\_flag$ variable of the dataset.

The results of the post-processing are included in the daily NetCDF files, for the Northern and Southern Hemisphere, respectively.

5 Results

A list of all output variables in the daily SIC files and a short description of them can be seen in Appendix A2. Examples of monthly means of the SIC and mean uncertainty can be seen in figure 6 and 7.

It is worth noticing that the coverage in figure 6 is complete and because of ESMR's wide swath width of 3100 km and its inclination, the North Pole is covered in contrast to the satellite microwave radiometers following NIMBUS 5 ESMR which have a "pole hole". The area covered by multiyear ice in the central Arctic has lower SIC than the first-year ice regions. This is a consequence of the one channel SIC algorithm, which has an inherent ambiguity between SIC, ice type and emitting layer temperature variations. In figure 6 b) and 7 b) it can be seen that the uncertainties are largest near the ice edges, as expected. This is due to the re-sampling uncertainty which is dominating near the ice edge where T_B spatial variability is high. Coastal

regions also show higher uncertainties for this reason, since the land-spill-over correction is first applied to the SIC after the uncertainty estimations.
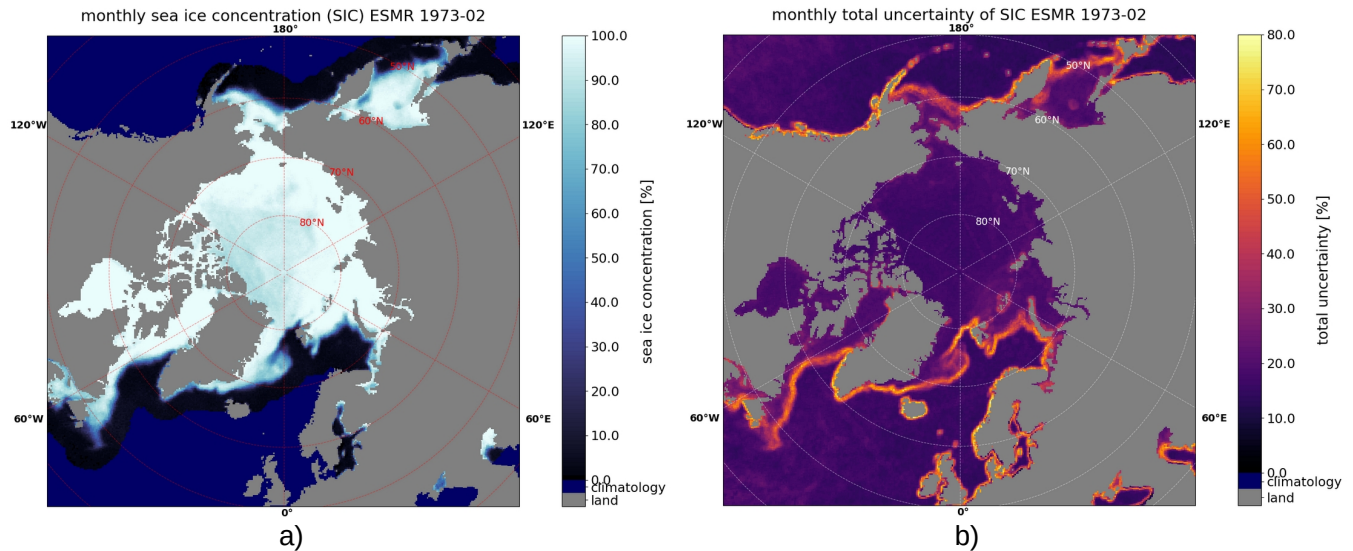
Figure 6. Monthly mean of a) SIC and b) uncertainty for February 1973 in the Northern Hemisphere. Water areas with no ice and uncertainty due to the ocean climatology are displayed in dark blue.

The SIC shows interesting sea ice features in the years 1972-1977. One such feature is the Odden ice tongue (Comiso et al., 2001) extending eastward from the East Greenland Current, visible in figure 6 (around 73°N, 0°E), while another feature is the Maud Rise Polynya (Jena et al., 2019), an open water area encircled by sea ice, in the Southern Hemisphere, which can be seen in figure 7 (around 65°S, 0°E). Both examples were much larger in extent in the 1970s and more frequently occurring than they are today (Comiso et al., 2001; Cheon and Gordon, 2019; Jena et al., 2019).

The daily coverage of valid data points that passed all filtering varies a lot through the ESMR operating period. While there is nearly full coverage for the first months, it gets much worse after the summer of 1975 when the instrument only recorded data every second day. An example of the poor coverage is shown for May 1976 in figure 8.

Monthly averaged SIC are derived to compare our results against other datasets. Only months with a 99% coverage have been used in the comparison, i.e. 99% of all grid points is at least covered once per month. From the monthly SIC, monthly mean SIE are calculated using a threshold of $c_{ice} > 30\%$. In figure 9 the ESMR data set (orange line) is shown together with the OSI-SAF CDR (blue line) for 1979-2022 (EUMETSAT, 2017a & EUMETSAT, 2017b) and the sea ice extent derived from NSIDC's NIMBUS 5 ESMR ice concentration product (green line) (Parkinson et al., 2004) using the same threshold for all products ($c_{ice} > 30\%$).

The comparison shows comparable SIE levels around 1980. In general, our ESMR data set has slightly higher monhtly SIE values than the NSIDC's ESMR product, even though the seasonal pattern is the same.
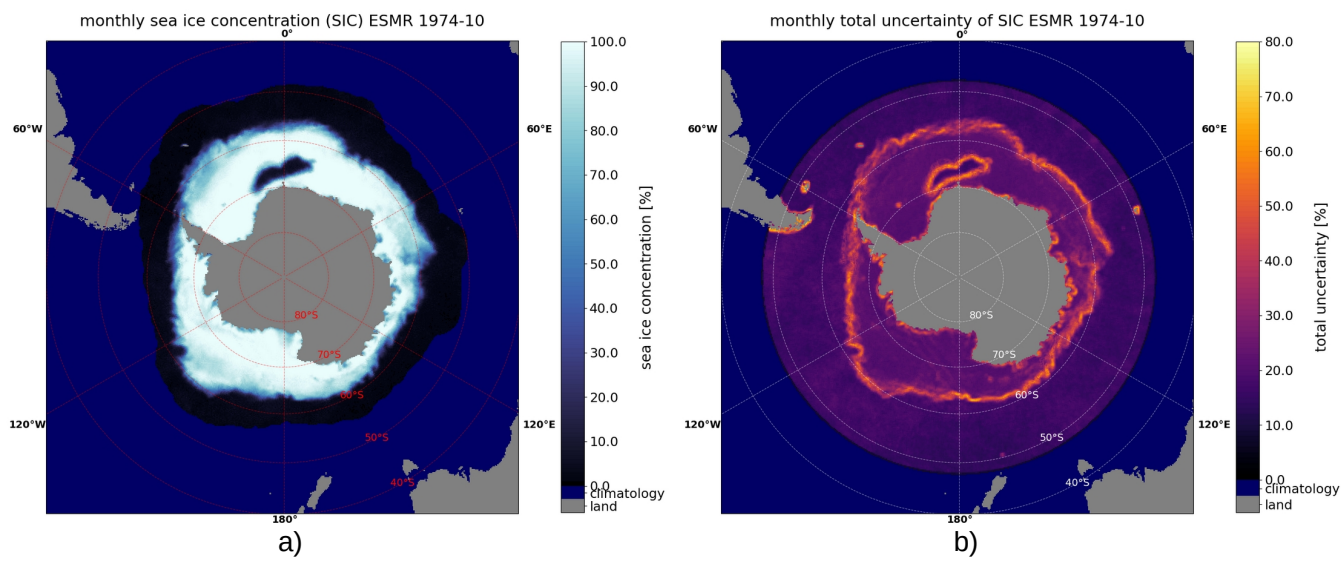
Figure 7. Monthly mean of a) SIC and b) uncertainty for October 1974 in the Southern Hemisphere. Water areas with no ice and uncertainty due to the ocean climatology are displayed in dark blue.
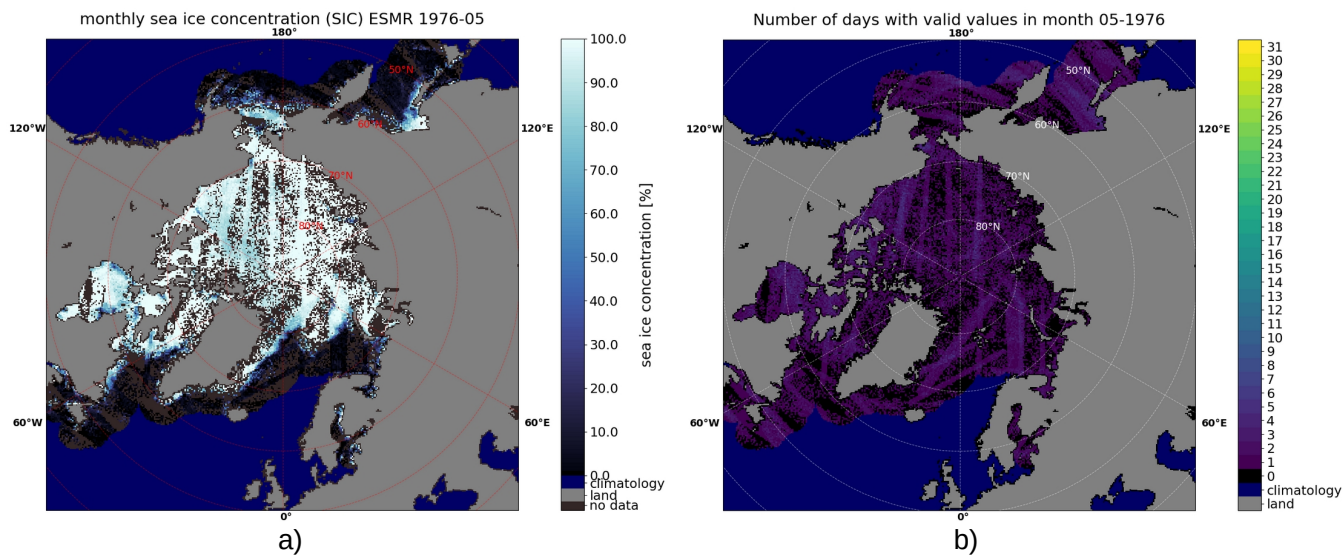
Figure 8. Example of poor monthly coverage for May 1976 in the Northern Hemisphere for a) the mean SIC and b) number of days with valid values. Water areas that would show a full daily coverage due to the ocean climatology are displayed in dark blue, to avoid misleading comparisons. Number of days with valid data are indicated by the colorbar.

The mean difference between our sea ice extent and that from NSIDC is 0.24 mill. km^2 in the Arctic and 0.59 mill. km^2 in the Antarctic for the whole data set.

For the Northern Hemisphere the SIE seems to have been similar in magnitude during the operational period of NIMBUS 5 ESMR 1972 to 1977 as during the operational period of NIMBUS 7 SMMR from 1978 to 1987, with the ESMR minimum extents being slightly higher than the SMMR ones. In the Southern Hemisphere the values of the second half of the 1970s seem to have been around the same magnitude as the largest SIE during the 2014/2015 season.

6   Discussions

Comparisons between different sea ice products and the new ESMR data set proved to be more difficult than initially expected, since not only the processing algorithms differ, but also the land masks, map projections and data set grids. We were not able to find two independent SIC data sets for 1978 onwards and 1972-77, which share exactly the same land mask.

Thus, it was decided at the beginning of the processing to use the same land mask as the OSI-420 product (1978 onwards) (EUMETSAT, 2020) for our ESMR data set, i.e. a 25 km equal area grid (EASE-2 version 2) land mask, to at least ensure a fair comparison between these two data sets. The NSIDC ESMR data set (green line in figure 9) used a different land mask with a polar stereographic projection (Parkinson et al., 2004), but was still compared to our ESMR data set.

The difference in SIE is therefore also influenced by the different projections of the data, however, the area difference between the projections is relatively small (only a few thousands of km^2), so even a re-projection is expected to yield minimal differences compared to differences caused by the use of different land masks. The comparison of different land masks is complicated by the varying sea ice extent, which exposes more or less land throughout its annual cycle, and thus changes the number of grid-points affected by the land mask.

The land masks land area differ between the OSI-SAF and NSIDC ESMR land mask. A comparison between the land mask land and ocean points between the NSIDC land mask and the OSI-SAF land mask showed a difference for the Northern Hemisphere of 460.000 km^2 (north of 60 degrees North), where the NSIDC has more land, while the difference is the opposite and much smaller in the Southern Hemisphere, with only 79.000 km^2 (south of 60 degrees South), where OSI-SAF's land mask has slightly more land. More land points in the land mask result in less available grid points for potential sea ice. The difference in the Southern Hemisphere sea ice extent is significantly larger and opposite to the expected contrast by the land mask difference. In the Northern Hemisphere it is not so clear how much of the SIE differences can be accounted to the land mask or algorithm differences. However, since the SIE differences are varying a lot and the differences in the Southern Hemisphere clearly cannot be explained by the land mask difference alone, it is likely that most of the SIE differences come from the algorithms and processing methods, such as the atmospheric correction and tie point calculation.

The blue curve in figure 9 is based on OSI-SAFs SIC products OSI-450 & OSI-430-b (EUMETSAT, 2017b & EUMETSAT, 2017a), corresponding to the SIE of the OSI-420 product (EUMETSAT, 2020), but instead of a 15% threshold, a 30% sea ice threshold has been used that matches the OSI-402-d sea ice extent product (EUMETSAT, 2017c).
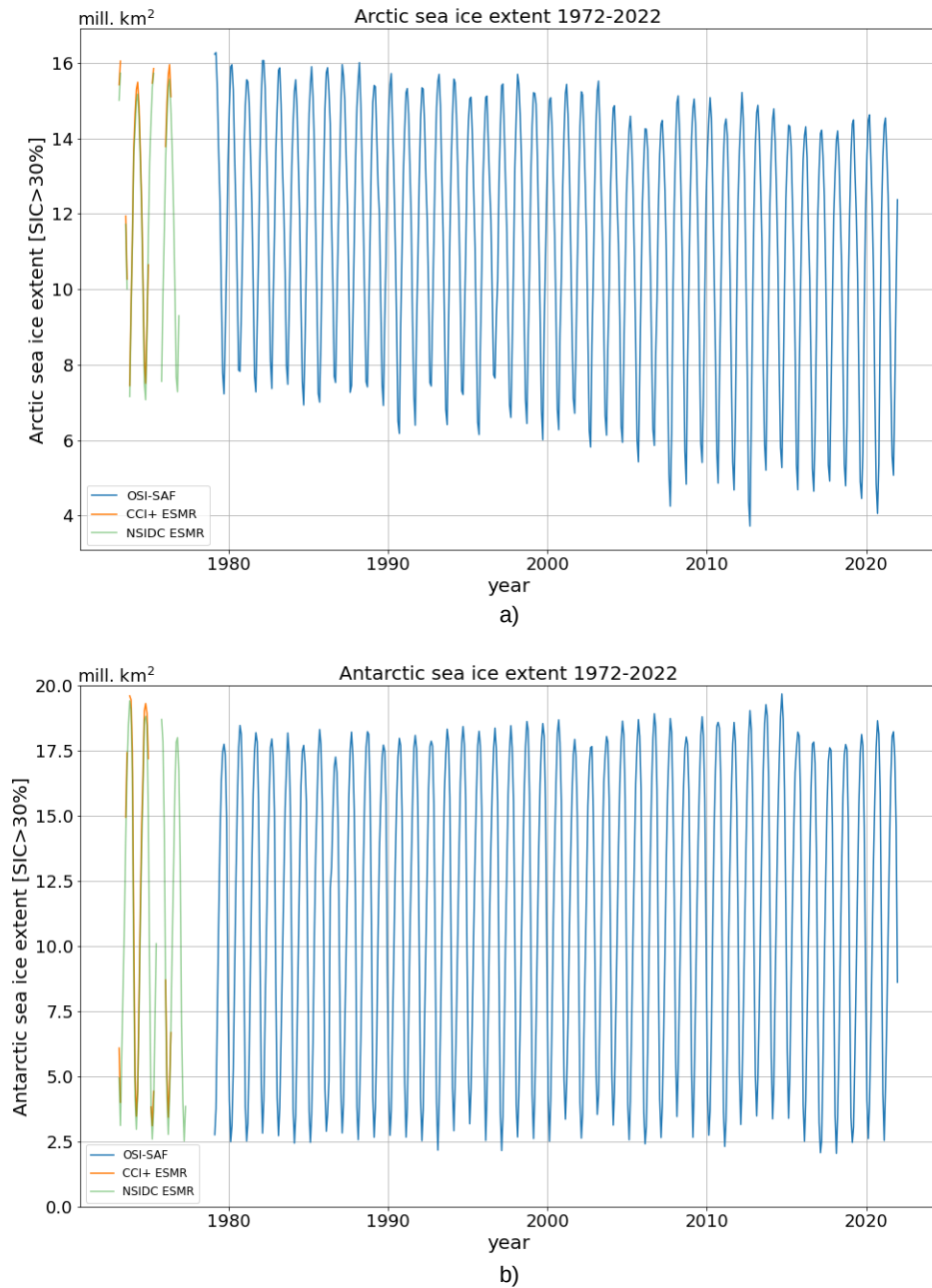
Figure 9. Monthly sea ice extent time series for the a) Arctic and b) Antarctic based on a $c_{ice} > 30\%$ threshold. The orange curve shows values of the ESMR dataset which have a 99% monthly coverage of the hemisphere, while the blue curve is based on the SIC products by OSI-SAF (EUMETSAT, 2017a & EUMETSAT, 2017b), where the $c_{ice} > 30\%$ threshold has been applied as at: EUMETSAT, 2017c . The green line represents NSIDC's ESMR SIC product.(Parkinson et al., 2004)

The 30% threshold, compared to the more common 15%, was better suited for a comparison between different ESMR SIE data sets due to the relatively high noise level, which can be seen from the total uncertainty in figure 5. The uncertainty algorithm has been applied for easier data assessment and comparability to other data sets.

A large amount of ESMR data is currently filtered out, and the 99% threshold for the inclusion to the monthly timeline is especially filtering out the second half of the ESMR data, where large data gaps occurred, as seen in figure 8.

The filters worked as expected and removed erroneous T_Bs from the raw data. To rescue more data points of the 20% of ESMR data files, that have been currently filtered out, a reprocessing of the data is planned. There are two approaches to improve the data selection during the next processing. One approach consists of changes to the set of filters, i.e. an adjustment of the filter thresholds, testing of different filters and a possible incorporation of an incidence angle dependency to the data selection. The other approach is to recalibrate some of the erroneous data files, which have shown some systematic offsets, to rescue whole swaths.

To reduce the uncertainty caused by atmospheric noise, the brightness temperatures were corrected with a RTM using several atmospheric parameters from NWP (ERA-5) data, such as water vapor and wind, as input. This correction showed a consistent reduction of the standard deviation of the brightness temperatures for water points in both hemispheres, as can be seen from figure 5. Over ice surfaces the correction was less steady, since the RTM is not describing all relevant processes related to the snow and ice, which are the main noise source over sea ice. Such processes include sea ice deformation, creation of leads or ridges, as well as changes in the snow layer of e.g. snow depth, snow density and, grain size, but also melting and refreezing, which influences scattering and emission processes inside the layer. Atmospheric noise caused by e.g. water vapor and cloud liquid water influences the TB over sea ice, but its influence is smaller, only around one third of the total noise (Tonboe et al., 2021). By correcting for atmospheric effects with ERA-5 data, we might have introduced some noise in the anglular dependency for the SIC, due to the use of an incident angle dependent emissivity in the RTM (figure 1 & table 1).

To avoid biases from the RTM and the NWP data, dynamical tie points have been used, which also calibrate the algorithm to seasonal variations and instrument drift. However, we currently use mean tie-points that are independent of the incident angle. Therefore, a possible improvement for a future version of the data set might be accomplished by using angle dependent tie-points instead.

Even after filtering the data for obvious errors it is clear that there are still issues with the absolute calibration of the instrument (Comiso and Zwally, 1980). For example, in 1973 after the hot-load anomaly the ocean T_B in the Southern Hemisphere is several Kelvin below the T_B level before the anomaly and in 1976 there is a dip in May and June followed by a sharp increase in T_B (Zwally et al., 1983). Low frequency (timescales $\geq$ days) T_B variations and regional variations on hemispherical scales are compensated by the dynamical SIC algorithm tie-points (Tonboe et al., 2016).

In spite of data gaps and calibration issues, the experimental NIMBUS satellite program was very successful. Applying modern processing methodologies, including dynamical tie-points and atmospheric noise reduction of the T_Bs, reduces the noise over both ice and open water consistently. This newly processed ESMR sea ice data-set extends the existing sea ice climate data record (CDR) with an important period from the 1970s. This extension of the SIE record contributes to the United

380 Nations Sustainable Development Goals (SDGs) related to climate change by providing more observations for longer-term assessments of Arctic and Antarctic sea ice changes.

7 Conclusions

In this paper we presented a new SIC data set covering 1972-1977, by using the ESMR data from the Nimbus-5 satellite. The data set consists of daily netCDF files for the Northern and Southern Hemispheres, respectively. SIC and associated
385 uncertainties are included in the data set. The uncertainties and choice of same land mask, spatial grid and projection as for EUMETSATs SIC CDR make comparisons between the time periods easier.

The most important findings can be summarized as:

A comparison to NSIDC's ESMR SIC product and the OSI-SAF CDR was presented. While the seasonal pattern is very similar to NSIDC's ESMR SIC product, our product shows systematic larger SIE values, which can not be explained by
390 differences between land masks alone. For the Northern Hemisphere our SIE values are matching the levels of the 1980s of the OSI-SAF CDR with the same land mask, while values of the Southern Hemisphere have been larger in the 1970s than in the 1980s.

Uncertainty variables have been included in our ESMR data set for better data assessment and easier comparison to other data sets.

395 Atmospheric noise has been reduced with the use of an RTM and the ERA5 atmospheric data.

Dynamical tie-points were used to avoid biases from the RTM and NWP data as well as to adjust to seasonal variability and instrument biases.

Data availability.

The newly processed ESMR data are released through the ESA CCI Open Data Portal:
400 https://climate.esa.int/en/odp/#/project/sea-ice
DOI: http://dx.doi.org/10.5285/34a15b96f1134d9e95b9e486d74e49cf (Tonboe et al., 2023)

Appendix A

A1

Table A1: The table is showing the data variables in the processing input NetCDF file and a description of each variable

Satellite variables	
Time	Time of data [year, month, day, hour, minute, second]
Brightness_temperature	Brightness temperature of the 78 scan spots [Kelvin x 10]
Latitude	latitude of the 78 scan spots [degrees x 10]
Longitude	longitude of the 78 scan spots [degrees x 10]
Pitch_fine_error	Pitch fine error [degrees x 10]
Roll_fine_error	Roll fine error [degrees x 10]
RMP_rate	RMP indicated rate high [x 10]
NADIR_LAT	Sub-satellite latitude [degrees x 10]
NADIR_LON	Sub-satellite longitude [degrees x 10]
Height	Satellite height [km]
Digital_b	A set of 1 bit status words to indicate the position of each of the command relays (users guide p. 83)
Status_indicator_1	A bit status word
Status_indicator_2	A bit status word
Data_source	A bit status word
Beam_position	A bit status word
PGM_id	Unique identification number assigned to program that prepared tapes
HOT_MEAN	Hot load mean [x 10]
HOT_RMS	RMS of hot load [x 100]
COLD_MEAN	Cold load mean [x 10]
COLD_RMS	RMS of cold load [x 100]
MUX_1	Average antenna temperature
MUX_2	Average phase shifter temperature
MUX_3	Ferrite switch temperature
MUX_4	Ambient load temperature
MUX_5	Reference load temperature
MUX_6	Automatic Gain Control
Analog_0	Analog signals (voltages)
Analog_1	Analog signals (voltages)
...	...
Analog_15	Analog signals (voltages)

ERA5 variables	
u10	u component of the wind speed at 10 m (parallel to latitude) $[ms^{-1}]$
v10	v component of the wind speed at 10 m (parallel to longitude) $[ms^{-1}]$
t2m	2 m air temperature [K]
istl1	Ice internal temperature [K]
...	...
istl4	Ice internal temperature [K]
lsm	Land-sea-mask
msl	Mean sea level pressure [hPa]
siconc	Sea ice concentration [0-1]
sst	Sea surface temperature [K]
skt	Skin temperature [K]
tcw	Total column water $[kgm^{-2}]$
tcwv	Total column water vapor $[kgm^{-2}]$
era_time	Valid time for analysis

Table A2: The table shows the output variables stored in the daily NetCDF files and a description of each variable

Output variables	
ice_conc	filtered sea ice concentration using atmospheric correction of brightness temperatures and open water filters [%]
raw_ice_conc_values	raw sea ice concentration estimates as retrieved by the algorithm [%]
total_standard_error	total uncertainty (one standard deviation) of sea ice concentration [%]
smearing_standard_error	smearing uncertainty of sea ice concentration [%]
algorithm_standard_error	algorithm uncertainty of sea ice concentration [%]
status_flag	status flag bits for the sea ice concentration as described in table 4
Tb_corr	corrected brightness temperatures [K]
Tb	uncorrected brightness temperatures [K]
time	Time of data [year, month, day]
xc	x coordinate of projection [km]
xy	y coordinate of projection [km]
lat	Latitude [degrees]
lon	Longitude [degrees]

Table A3. The table is showing the missing dates

			Missing dates			
Year	Jan	Feb	Mar	Apr	May	Jun
1972						
1973	-	28	1-31	1-30	1-27	-
1974	12-15	10-11	24-31	1-5	14-15	-
1975	-	21	24,31	1-8,16-30	1-2	3-30
1976	1,3,5,7, 9,13,15,17, 19,21,23,27	2,6,12, 14,16,18, 22,24,26,28	1,3,5,7,9, 11,13,15,19, 21,23,25,27,31	2,4,6,8,10, 12,14,16,18,20, 22,24,28,30	2,6,8, 10,12,20, 24,30	13,15,17, 19,21,23, 25,27,29
1977	9-18,23, 25,27,29,31	4,6,8,10, 12,14,16,18, 20-22,24,26,28	4,6,8,10, 12,14,16,20, 26,28,30-31	1-29	1,3,5,7,9,11-16	

Year	Jul	Aug	Sep	Oct	Nov	Dec
1972						31
1973	27-28	1-31	1-4,13-16,22-23	14-15	9-10,29-30	1,5,14-17
1974	17-19	1-8,13-14	-	22-23,25-27	1	-
1975	1-31	1-17,19,21-25, 27,29,31	5-6,8,10, 12,14,16,18, 20,22,24, 26,28,30	2,4,6-8, 10,12,14,18, 20,22,24,26	1,3,5,7,9,11, 13,15,17,19, 21,23,25,27,29	1,3,5,7,9,11, 13,15,17,19,21, 23,25,27,29,31
1976	1,3,5,7,9, 11,13,15,17,19,21, 23,25,27,29,31	2,4,6,8,10, 12,14,16,18,20, 22,24,26,28,30	1,5,11, 13,15,17, 23,25,27	1,3,5,7,9, 13,15,17,19,21, 23,25,27,29,31	2,4,6,8, 10,12,14,16, 18,20,22,24, 26,28,30	2,4,6,8, 10,12,14-18, 20,22,24,31
1977						

Author contributions. WK performed the experiments, investigated the data, developed software and wrote the manuscript with contributions from all authors. RT contributed to the conceptualization, methodology, software, investigation, original draft and review & editing of the manuscript, and provided supervision throughout the work. JS contributed with critical feedback that shaped the interpretation and presentation of the data and improved the manuscript through review & editing.

Competing interests. The authors declare no competing interests relevant to the work presented in this paper.

Acknowledgements. This work is part of the ESA Climate Change Initiative Programme (ESA CCI) Sea Ice CCI (Sea_Ice_cci) project and the Danish National Centre for Climate Research (NCKF) at the Danish Meteorological Institute (DMI). The authors would like to thank Tadea Veng, Roberto Saldo, Thomas Lavergne, Atle Sørensen and Leif Toudal Pedersen for their inputs and valuable feedback. We would also like to thank Imke Sievers, John Andrew Dawson, and Andreas Svejgaard Jensen for developing and testing the data filters described in section 2.

References

415 Andersen, S. & Tonboe, R. & Kern, S. & Schyberg, H.: Improved retrieval of sea ice total concentration from spaceborne passive microwave observations using Numerical Weather Prediction model fields: An intercomparison of nine algorithms. Remote Sensing of Environment. 104. 374-392. 10.1016/j.rse.2006.05.013, 2006.

Bell, B., Hersbach, H., Berrisford, P., Dahlgren, P., Horányi, A., Muñoz Sabater, J., Nicolas, J., Radu, R., Schepers, D., Simmons, A., Soci, C., Thépaut, J-N.: ERA5 hourly data on single levels from 1950 to 1978 (preliminary version). Copernicus Climate Change Ser-
420 vice (C3S) Climate Data Store (CDS), https://cds.climate.copernicus.eu/cdsapp#!/dataset/reanalysis-era5-single-levels-preliminary-back-extension?tab=overview , last access: 6 August 2021, 2020.

Bell, B., Hersbach, H., Simmons, A., Berrisford, P., Dahlgren, P., Horányi, A., et al. The ERA5 global reanalysis: Preliminary extension to 1950. Q J R Meteorol Soc, 147(741, 4186–4227. Available from: https://doi.org/10.1002/qj.4174 , 2021

Chapman, W. L. and Walsh, J. E.: Long-range prediction of regional sea ice anomalies in the Arctic, Weather Forecasting, 6, 271– 288,
425 https://doi.org/10.1175/1520-0434(1991)006<0271:LRPORS>2.0.CO;2 , 1991.

Cheon, W.G. and Gordon, A.L.: Open-ocean polynyas and deep convection in the Southern Ocean. Sci Rep 9, 6935, https://doi.org/10.1038/s41598-019-43466-2, 2019.

Comiso, J. C., and Zwally, H. J.: Correction for anomalous time dependent shifts in the brightness temperature from Nimbus 5 ESMR, NASA TM-82055, Greenbelt, Maryland, 18 pp., 1980.

430 Comiso, J. C., Cavalieri, D. J., Parkinson, C. L., and Gloersen, P.: Passive microwave algorithms for sea ice concentration: A comparison of two techniques: Remote Sensing of Environment [Remote Sens. Environ.], vol. 60, no. 3, pp. 357-384, Jun 1997.

Comiso, J. C., Wadhams, P., Pedersen, L. T., and Gersten, R.A.: Seasonal and interannual variability of the Odden ice tongue and a study of environmental effects. Journal of Geophysical Research. 106. 9093-9116. 10.1029/2000JC000204, 2001.

ESA Climate Office, CCI+ Sea Ice ECV ESMR Sea Ice Concentration Product User Guide for ESMR (PUG-ESMR), Reference: D4.2-
435 ESMR, Issue 1.1, https://climate.esa.int/en/projects/sea-ice/Sea-Ice-Key-Documents/ , last access: 20 December 2023, 2022.

EUMETSAT Ocean and Sea Ice Satellite Application Facility, Global sea ice concentration interim climate data record 2016-onwards (v2.0, 2017), OSI-430-b, (Data extracted from OSI SAF FTP server/EUMETSAT Data Center : ([2016-2022],) ([global],)) last access: 19 October 2022, 2017a.

EUMETSAT Ocean and Sea Ice Satellite Application Facility, Global sea ice concentration climate data record 1979-2015 (v2.0, 2017),
440 OSI-450, doi: 10.15770/EUM_SAF_OSI_0008, (Data extracted from OSI SAF FTP server/EUMETSAT Data Center: ([1979-2015],) ([global],)) last access: 19 October 2022, 2017b.

EUMETSAT Ocean and Sea Ice Satellite Application Facility, Global Sea Ice Edge product, OSI-402-d, osi-saf.eumetsat.int, last access: 19 October 2022, 2017c.

EUMETSAT Ocean and Sea Ice Satellite Application Facility, Sea ice index 1979-onwards (v2.1, 2020), OSI-420, Data extracted from OSI
445 SAF FTP server: 1979-2019, Northen & Southern Hemisphere, last access: 19 October 2022, The OSI SAF Sea Ice Index v2.1 is made available at https://osisaf-hl.met.no/v2p1-sea-ice-index, 2020.

Ferreira, D., Marshall, J., Bitz, C. M., Solomon, S., and Plumb, A.: Antarctic Ocean and Sea Ice Response to Ozone Depletion: A Two-Time-Scale Problem, Journal of Climate, 28(3), 1206-1226. ,https://doi.org/10.1175/JCLI-D-14-00313.1, 2015.

Fogt, R. L., Sleinkofer, A. M., Raphael, M. N., and Handcock, M. S.: A regime shift in seasonal total Antarctic sea ice in the twentieth
450 century. Nature Climate Change 12, 54-62, https://doi.org/10.1038/s41558-021-01254-9, 2022.

Hersbach, H., Bell, B., Berrisford, P., Hirahara, S., Horányi, A., Muñoz-Sabater, J., Nicolas, J., Peubey, C., Radu, R., Schepers, D., Simmons, A., Soci, C., Abdalla, S., Abellan, X., Balsamo, G., Bechtold, P., Biavati, G., Bidlot, J., Bonavita, M., and Thépaut, J.-N.: The ERA5 global reanalysis. Quarterly Journal of the Royal Meteorological Society. https://doi.org/10.1002/qj.3803, 2020.

Jena, B., Ravichandran, M., and Turner, J.: Recent reoccurrence of large open-ocean polynya on the Maud Rise seamount. Geophysical
455   Research Letters, 46, 4320– 4329. https://doi.org/10.1029/2018GL081482, 2019.

Knight RW. Introduction to a New Sea-Ice Database. Annals of Glaciology. 1984;5:81-84. doi:10.3189/1984AoG5-1-81-84 , 1984

Kongoli, C., Boukabara, S.-A., Yan, B., Weng, F., and Ferraro, R.: A New Sea-Ice Concentration Algorithm Based on Microwave Surface Emissivities—Application to AMSU Measurements, IEEE Transactions on Geoscience and Remote Sensing, vol. 49, no. 1, pp. 175-189, doi: 10.1109/TGRS.2010.2052812, 2011.

460 Lavergne, T., Sørensen, A. M., Kern, S., Tonboe, R., Notz, D., Aaboe, S., Bell, L., Dybkjær, G., Eastwood, S., Gabarro, C., Heygster, G., Killie, M. A., Brandt Kreiner, M., Lavelle, J., Saldo, R., Sandven, S., and Pedersen, L. T.: Version 2 of the EUMETSAT OSI SAF and ESA CCI sea-ice concentration climate data records, The Cryosphere, 13, 49–78, https://doi.org/10.5194/tc-13-49-2019, 2019.

Markus, T., Cavalieri, D. J.: The AMSR-E NT2 sea ice concentration algorithms: its basis and implementation. Journal of the Remote Sensing Society of Japan 29(1), 216-225, 2009.

465 Meissner, T. and Wentz, F.: AMSR Ocean Algorithm, Algorithm Theoretical Basis Document (ATBD) Version 2, https://eospso.gsfc.nasa.gov/sites/default/files/atbd/atbd-amsr-ocean.pdf, 2000.

Meissner, T. and Wentz, F.: The emissivity of the ocean surface between6 and 90 ghz over a large range of windspeeds and earth incidence angles. Ieee Transactions on Geoscience and Remote Sensing, 50(8):3004–3026, 2012.

NASA: The NIMBUS 5 data catalog, data orbits 8843 - 9660, volume 12, final report, 1. Oct. - 30. Nov. 1974, NASA CR 157882, 1974.

470 NASA Goddard Space Flight Center (GSFC), ESMR/Nimbus-5 Level 1 Calibrated Brightness Temperature V001, Greenbelt, MD, USA, Goddard Earth Sciences Data and Information Services Center (GES DISC), accessed [26-06-2019], https://disc.gsfc.nasa.gov/datacollection/ESMRN5L1_001.html, last access: 26 June 2019, 2016.

Onarheim, I., Eldevik, T., Smedsrud, L., and Stroeve, J.C.: Seasonal and Regional Manifestation of Arctic Sea Ice Loss. Journal of Climate. 31. 10.1175/JCLI-D-17-0427.1, 2018.

475 Parkinson, C. L., Comiso, J. C., Zwally, H. J., Cavalieri, D. J., Gloersen, P., Campbell, W. J.: Arctic sea ice, 1973-1976: satellite passive-microwave observations. NASA special publications. NASA SP-489, 1987.

Parkinson, C. L., J. C. Comiso, and H. J. Zwally. Nimbus-5 ESMR Polar Gridded Brightness Temperatures, Version 2 [Data Set & User Guide]. Boulder, Colorado USA. NASA National Snow and Ice Data Center Distributed Active Archive Center. https://doi.org/10.5067/CIRAYZROIYF9. Date Accessed 12-18-2023, 1999.

480 Parkinson, C. L., Comiso, J. C., and Zwally, H. J., edited by Meier, W., and Stroeve, J.: Nimbus-5 ESMR Polar Gridded Sea Ice Concentrations, Version 1. Boulder, Colorado USA. NASA National Snow and Ice Data Center Distributed Active Archive Center. doi: https://doi.org/10.5067/W2PKTWMTY0TP. last access: 14 November 2022, 2004.

Rayner, N. A., Parker, D. E., Horton, E. B., Folland, C. K., Alexander, L. V., Rowell, D. P., Kent, E. C., and Kaplan, A.: Global analyses of sea surface temperature, sea ice, and night marine air temperature since the late nineteenth century, J. Geophys. Res., 108, 4407,
485   doi:10.1029/2002JD002670, D14, 2003.

Sabatini, R.R.(ed.): The Nimbus 5 user's guide: NASA Goddard Space Flight Center (U.S. Govt. Printing Office), 1972.

Schanda, E.: Physical Fundamentals of Remote Sensing. Springer-Verlag, Berlin Heidelberg., https://doi.org/10.1007/978-3-642-48733-0, 1986.

Schroeter, S., O'Kane, T., and Sandery, P.: Antarctic sea ice regime shift associated with decreasing zonal symmetry in the Southern Annular Mode. https://doi.org/10.5194/tc-17-701-2023., 2023.

Singh, H. A., Polvani, L. M., and Rasch, P. J.: Antarctic sea ice expansion, driven by internal variability, in the presence of increasing atmospheric CO2. Geophysical Research Letters, 46 https://doi.org/10.1029/2019GL083758, 2019.

Stammerjohn, S. E., Martinson, D. G., Smith, R. C., Yuan, X., and Rind, D.: Trends in Antarctic annual sea ice retreat and advance and their relation to El Niño–Southern Oscillation and Southern Annular Mode variability, J. Geophys. Res., 113, C03S90, doi:10.1029/2007JC004269, 2008.

Stroeve, J.C. and Notz, D.: Changing state of Arctic sea ice across all seasons. Environmental Research Letters. 13. 10.1088/1748-9326/aade56, 2018.

Sun, S., and Eisenman, I.: Observed Antarctic sea ice expansion reproduced in a climate model after correcting biases in sea ice drift velocity. Nat Commun 12, 1060 (2021), https://doi.org/10.1038/s41467-021-21412-z, 2021.

Svendsen, E., Kloster, K., Farrelly, B., Johannessen, O. M., Johannessen, J. A., Campbell, W. J., Gloersen, P., Cavalieri, D., and Mätzler, C.: Norwegian Remote Sensing Experiment: Evaluation of the Nimbus 7 scanning multichannel microwave radiometer for sea ice research, J. Geophys. Res., 88(C5), 2781– 2791, doi:10.1029/JC088iC05p02781, 1983.

Thompson, D. W. J. and Solomon, S.: Interpretation of Recent Southern Hemisphere Climate Change, Science, Vol.296, 5569, p.895-899, https://doi.org/10.1126/science.1069270, 2002.

Titchner, H. A., and Rayner, N. A.: The Met Office Hadley Centre sea ice and sea surface temperature data set, version 2: 1. Sea ice concentrations, J. Geophys. Res. Atmos., 119, 2864– 2889, doi:10.1002/2013JD020316, 2014.

Tonboe, R. T.: The simulated sea ice thermal microwave emission at window and sounding frequencies. Tellus A, 62(3):333–344, 2010.

Tonboe, R. T., Eastwood, S., Lavergne, T., Sørensen, A. M., Rathmann, N., Dybkjær, G., Pedersen, L. T., Høyer, J. L., and Kern, S.: The EUMETSAT sea ice concentration climate data record, The Cryosphere, 10, 2275–2290, https://doi.org/10.5194/tc-10-2275-2016, 2016.

Tonboe, R., Nandan, V., Mäkynen, M., Pedersen, L., Kern, S., Lavergne, T., Øelund, J., Dybkjær, G., Saldo, R., and Huntemann, M.: Simulated Geophysical Noise in Sea Ice Concentration Estimates of Open Water and Snow-Covered Sea Ice. IEEE Journal of Selected Topics in Applied Earth Observations and Remote Sensing. PP. 1-1. 10.1109/JSTARS.2021.3134021, 2021.

Tonboe, R.T., Kolbe, W.M., Toudal Pedersen, L., Lavergne, T., Sørensen, A., and Saldo, R.: ESA Sea Ice Climate Change Initiative (Sea_Ice_cci): Nimbus-5 ESMR Sea Ice Concentration, version 1.0. NERC EDS Centre for Environmental Data Analysis, 03 February 2023. doi:10.5285/34a15b96f1134d9e95b9e486d74e49cf. http://dx.doi.org/10.5285/34a15b96f1134d9e95b9e486d74e49cf, 2023.

Turner, J., Comiso, J. C., Marshall, G. J., Lachlan-Cope, T. A., Bracegirdle, T., Maksym, T., Meredith, M. P., Wang, Z., and Orr, A.: Non-annular atmospheric circulation change induced by stratospheric ozone depletion and its role in the recent increase of Antarctic sea ice extent, Geophys. Res. Lett., 36, L08502, doi:10.1029/2009GL037524, 2009.

Ulaby, F. T., Moore, M. K., and Fung, A. K.: Microwave Remote Sensing, Active and Passive, Vol. 3, Artech House, Norwood, MA, 1986.

Veng, T.: Mapping of sea ice using NIMBUS 5 ESMR satellite data. Master thesis. DTU Space. 2021. https://findit.dtu.dk/en/catalog/6059da9cd9001d016554ff7a, 2021.

Walsh, J. E. 1978. A data set on Northern Hemisphere sea ice extent, 1953-76.World Data Center-A for Glaciology, Boulder, Colorado, Glaciological Data Report GD-2, p. 49-51

Walsh, J. E. and Johnson, C. M.. 1979. An analysis of Arctic sea ice fluctuations, 1953-1977. J. Phys. Oceanogr, 9(3), 580-591. https://doi.org/10.1175/1520-0485(1979)009%3C0580:AAOASI%3E2.0.CO;2 , 1979

Walsh, J. E. and Chapman, W. L.: 20th-century sea-ice variations from observational data, Ann. Glaciol., 33, 444–448, https://doi.org/10.3189/172756401781818671 , 2001

Walsh, J. E., Fetterer, F., Stewart,J. S., and Chapman, W. L.: A database for depicting Arctic sea ice variations back to 1850, Geographical Review, 107:1, 89-107, DOI: 10.1111/j.1931-0846.2016.12195.x, 2017.

530   Walsh, J. E., Chapman, W. L., Fetterer, F., and Stewart, J. S.: Gridded Monthly Sea Ice Extent and Concentration, 1850 Onward, Version 2 [Data Set]. Boulder, Colorado USA. National Snow and Ice Data Center. https://doi.org/10.7265/jj4s-tq79. Last Access: 14 November 2022, 2019.

Wang, G., Hendon, H. H., Arblaster, J.M. et al.: Compounding tropical and stratospheric forcing of the record low Antarctic sea-ice in 2016. Nat Commun 10, 13 (2019). https://doi.org/10.1038/s41467-018-07689-7, 2019.

535   Wentz, F. J.: A model function for ocean microwave brightness temperatures, J. Geophys. Res., 88(C3), 1892– 1908, doi:10.1029/JC088iC03p01892, 1983.

Wentz, F. J.: A well-calibrated ocean algorithm for special sensor microwave / imager, J. Geophys. Res., 102(C4), 8703– 8718, doi:10.1029/96JC01751, 1997.

Zwally, H. J., Comiso, J. C., Parkinson, C.L., Campbell,W. J., Carsey, F. D., and Gloersen, P.: Antarctic sea ice 1973-1976: Satellite passive
540   microwave observations. NASA SP-459, Washington DC, pp. 206, 1983.